Phys. Status Solidi B **246**, No. 11–12, 2683–2688 (2009) / **DOI** 10.1002/pssb.200982306

physica status solidi b
www.pss-b.com
basic solid state physics

Probing exciton propagation and quenching in carbon nanotubes with near-field optical microscopy

Carsten Georgi[1], Miriam Böhmler[1], Huihong Qian[1], Lukas Novotny[2], and Achim Hartschuh[*,1]

[1] Department Chemie und Biochemie and CeNS, Ludwig-Maximilians-Universität München, 81377 München, Germany
[2] University of Rochester, The Institute of Optics, Rochester, New York 14627, USA

Received 30 April 2009, accepted 17 August 2009
Published online 21 October 2009

PACS 61.48.De, 68.37.Uv, 71.35.Cc, 78.67.Ch

[*] Corresponding author: e-mail achim.hartschuh@cup.uni-muenchen.de, Phone: ++49 (89) 2180-77515, Fax: ++49 (89) 2180-77188

We report on near-field optical imaging of single-walled carbon nanotubes (SWNTs), observing photoluminescence (PL) quenching at nanotube ends and defects. The extension of reduced PL reflects the exciton diffusion length of about 100 nm, which can be directly visualized with our technique. Additionally, we model the complete imaging process, including exciton diffusion and tip-induced rate enhancement, for a deeper understanding of the experimental data and the determination of, e.g. diffusion length and tip enhancement from near-field PL images.

1 Introduction Based on their exceptional optical properties, carbon nanotubes will eventually play an important role as nanometer-scale building-blocks for optoelectronics, nanoelectronics and biosensing applications [1, 2]. Optical excitation of semiconducting nanotubes generates excitons that determine virtually all light-based applications. Exciton energies and decay dynamics can be investigated on the single nanotube level using photoluminescence (PL) microscopy and spectroscopy. PL of semiconducting nanotubes arises from radiative exciton recombination with rather short decay times in the range of few tens of picoseconds [3–9]. Observation of PL energies and dynamics from single nanotubes provides access to the properties of excitonic states in SWNTs with specific chirality (n,m) [10–12]. Compared to diffraction limited conventional confocal microscopy, near-field microscopy offers high spatial resolution optical information resolving relevant length scales, such as the exciton diffusional range [13, 14].

In this work we use tip-enhanced near-field optical microscopy (TENOM) [15–18] as a tool to visualize and characterize PL along nanotubes and evaluate signatures of exciton diffusion in the images.

2 Experimental Our setup for near-field optical microscopy and spectroscopy is based on an inverted confocal microscope with an x, y scan stage for raster scanning a transparent sample [15–17]. A sharp gold tip is positioned in the focus of the laser beam and maintained above the sample surface at a distance of ≈ 2 nm by means of a sensitive shear-force feedback mechanism [19]. The laser beam with a wavelength of 632.8 nm is radially polarized, which leads to a strong longitudinal field component oriented parallel to the tip axis after focusing with a high numerical aperture (NA = 1.4) objective. This longitudinal field is needed to efficiently excite the tip and generate enhancement.

The optical signal is then detected either by a combination of a spectrograph and a cooled charged coupled device (CCD) or by a single-photon counting avalanche photodiode (APD) after spectral filtering. The silicon based CCD and APD detect light up to wavelengths of 1050 nm. A near-field optical image is established by raster scanning the sample and simultaneously recording topographic and optical signals at each image pixel.

The sample studied in this paper was made by spin-coating DNA-wrapped CoMoCAT SWNTs in solution on a freshly cleaved thin layer of mica glued on a glass cover slide [20–23].

Upon excitation with the laser at 632.8 nm, the SWNTs show resonant Raman scattering when the energy of the incident or scattered photon is resonant with an optical transition in the nanotube, depending on the particular

chirality (n,m) [24]. Without resonance, the Raman signal is barely detectable. The strongest Raman band (*G*-band) appears at around 700 nm. For semiconducting SWNTs, PL in the near-infrared range above 800 nm can be observed. The PL energy also depends on the nanotube chirality as it reflects the lowest optical transition. Simultaneous observation of Raman and PL in our setup is limited to few chiralities as e.g. (9,1) or (8,3).

3 Near-field imaging of SWNT: Modelling and understanding exciton diffusion

3.1 Exciton mobility and quenching The excitons in SWNTs are highly mobile and can travel around 90–110 nm along the nanotube before recombining and eventually emitting a photon [13, 14]. This exciton motion is a one-dimensional diffusion process and can be described by a 1D random walk model or by analytically solving the diffusion equation [25]. The diffusion length L, diffusion coefficient D and exciton lifetime τ are connected by $L^2 = 2D\tau$. At the nanotube ends, excitons are expected to be efficiently quenched due to localized states within the bandgap arising from dramatic band modifications related and confined to the ends [26–29]. Charge carrier doping has also been predicted to quench excitons in a nonradiative Auger-recombination process involving the exciton and a single hole or electron [30, 31]. Thus, whenever an exciton reaches an end or a quenching defect during its lifetime, it will recombine nonradiatively and not contribute to the measured PL. Due to the exciton mobility, the PL is gradually reduced around the defect on a length scale of the diffusion length ($\sim$100 nm). With TENOM, offering a spatial resolution of down to 10 nm, this effect can be directly observed which is subject of this paper. In Ref. [12], we reported on the first observations of reduced PL near nanotube ends on length scales of 50–90 nm. Here we provide new experimental data and establish a theoretical model for the quantitative description of near-field images and the role of mobility and localized quenching sites.

3.2 Modelling PL imaging of carbon nanotubes In order to extract information on the exciton mobility from TENOM images, it is necessary to understand and model the underlying imaging formation process. The tip enhancement that leads to the high spatial resolution is based on the enhancement of the excitation rate k_{ex} and the radiative rate k_{rad}, thus affecting both exciton lifetime and diffusion. At very close tip-sample distances, the metallic tip provides additional nonradiative recombination pathways and can quench excitons by increasing also the nonradiative decay rate. These rate enhancement effects leading to strongly reduced fluorescence lifetimes at nanometer-scale tip-sample distances have been demonstrated for single molecule fluorescence [32]. In the case of SWNTs on substrates with low intrinsic quantum yield ($10^{-3} - 10^{-2}$), the effect of quenching is less important [15].

The PL signal detected in the far-field originates from either the far-field excitation or the enhanced near-field beneath the tip. It is always the sum of tip-independent far-field background and the desired near-field contributions, with a contrast depending on the tip enhancement factor. For moderate enhancement, the broad far-field components are clearly visible (see Fig. 1(a)) and cannot easily be separated from the near-field. Simulating the imaging and comparing with experimental data enables us to estimate enhancement factors, identify far-field components and draw conclusions regarding the underlying nanotube properties.

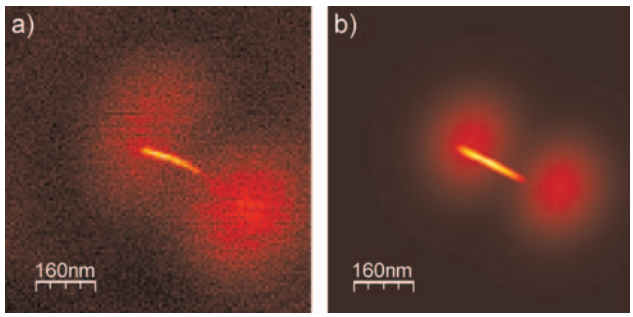

Figure 1 (online colour at: http://www.pss-b.com) (a) Experimental and (b) simulated near-field PL image of a short luminescent nanotube with 200 nm length. Due to the moderate field enhancement achieved with this tip, the two sidelobes from the far-field background are clearly visible. This pattern arises from the polarization components aligned along the nanotube in the radially polarized laser focus. The near-field is slightly off-centre, because the tip was not perfectly centred in the focus but shifted by about 70 nm.

Our simulations are based on a one-dimensional random walk model, where the nanotube is discretized into small segments Δx of 3–5 nm. The temporal evolution of the spatial exciton population is calculated in timesteps of about $\tau/400$, during which the excitons travel the aforementioned segment length Δx, with equal probability forwards or backwards. The initial exciton population $n(x, 0)$ along the nanotube is given by the intensity distribution of the focal fields and the tip enhanced contribution in the centre of the focus. During each timestep, the excitons travel one step $\pm\Delta x$ and decay according to the sum of radiative and nonradiative rate.

$$n(x, t + \Delta t) = \tfrac{1}{2}[n(x - \Delta x, t) + n(x + \Delta x, t)] \times [1 - k_{rad}(x)\Delta t - k_{nrad}(x)\Delta t].$$

The decay rates are locally varying and increased beneath the tip. At the nanotube ends and quenching defects, the exciton population $n(x, t)$ is set to 0, corresponding to an infinitely high nonradiative rate at these points. The PL is collected during each timestep according to the respective radiative rate $k_{rad}(x)$ and confocal detection sensitivity $\det(x)$ along the whole nanotube and summed up for all segments. For our setup, the detection sensitivity is modelled with a Gaussian profile determined by the diffraction limited far-field resolution (FWHM = 250 nm).

$$\mathrm{PL}(t) = \sum_x k_{rad}(x)\,\Delta t\, n(x, t)\,\det(x).$$

The cw-excitation is reproduced by summing up the PL for each timestep until complete decay of the exciton population. Exciton–exciton annihilation at high exciton densities is not considered and not expected for laser intensities of 10–25 μW used in the experiment. Images are calculated by repeating this procedure for every image pixel, i.e. the tip and centre of focus change their position with respect to the nanotube, just as for the experiment.

The focal field distribution is calculated according to Ref. [33], using only the in-plane components polarized along the nanotube axis, which is a two-lobe pattern for the radially polarized laser focus. The local near-field intensity resulting from the maximum tip-enhanced excitation rate $k_{ex}^{tip} = f^{ex} k_{ex}^{0}$ underneath the tip is modelled by a narrow Gaussian function with FWHM = 15–35 nm, depending on the tip width. The tip width can be taken directly from the experimental PL images as the width of the near-field signal. The same Gaussian function is used for the enhanced radiative rate $k_{rad}^{tip} = f^{rad} k_{rad}^{0}$ and much narrower (~5 nm) for the enhanced nonradiative rate $k_{nrad} = q\, k_{rad}^{tip}$, since this is only present for very small tip distances [34].

Figure 1 shows the experimental and simulated PL images for a SWNT which luminesces along a length of 200 nm. The excitation rate and radiative rate enhancement (f^{ex} and f^{rad}) were both set to a moderate value of 4 to reproduce the measured data with clearly visible far-field contributions. The two weak side-lobes correspond to the field components of the laser focus polarized along the nanotube axis, convoluted with a short luminescent nanotube, quite similar to the response of a point dipole. The near-field signal induced by the tip is shifted by about 70 nm from the centre, because the tip was not ideally centred in the focus. Taking this into account for the excitation intensity distribution, the image can be well reproduced. The fade-out of near-field PL towards the ends, due to exciton mobility, is apparent and is in close agreement with the simulation based on a diffusion length of 100 nm, recently reported from confocal experiments [13, 14]. Thus, the nanotube appears always shorter in the near-field PL image than in the corresponding topography[12].

As can be seen from the images in Fig. 1, signal enhancement factors derived from far-field to near-field ratios at a single sample position are not well defined. In particular, for short 1D structures (<700 nm), the effects of far-field excitation pattern and exciton mobility strongly affect the local ratios. Simulating the imaging process allows to determine more reliable values.

In Fig. 2(a), we show another example for the PL of a short nanotube with a length of 120 nm, derived from the simultaneously acquired topography (not shown). The near-field PL intensity along the nanotube, together with the simulated cross-section, is depicted in Fig. 2(b). There is no obvious far-field background visible, due to a near-field intensity enhancement of at least 10. The limited signal-to-noise ratio does not allow for a perfect match between simulation and experiment, but the simple model with quenching only at the ends can reproduce the PL profile. Influences of tip position stability, PL blinking or local DNA wrapping and other environmental effects cannot be taken into account.

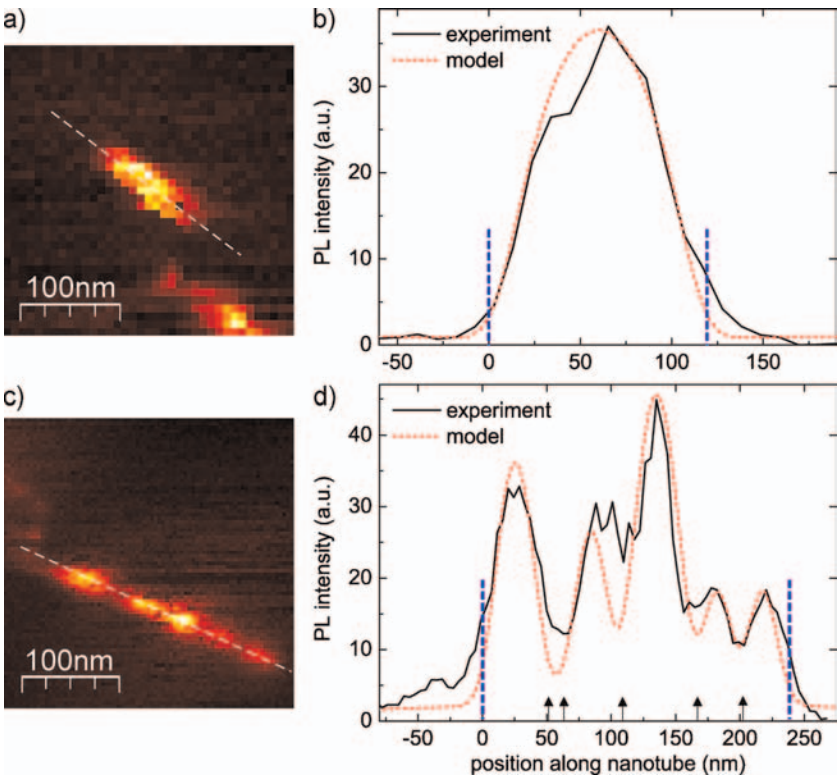

Figure 2 (online colour at: http://www.pss-b.com) Near-field PL images of a short nanotube with 120 nm length (a) and a 240 nm long nanotube showing distinct PL variations (c). Figs. (b) and (d) show the respective PL intensity cross-sections along the nanotubes (along white dashed lines in (a) and (c)) together with the simulated PL distributions. We assumed complete quenching at the ends (positions marked with blue dashed lines) and, for the second tube, five additional defects (black arrows). This simple modelling is already in reasonable agreement with the experimental data, supporting our picture of exciton diffusion.

For longer nanotubes, we often observe extended PL along the whole tube with quenching apparent only at the ends, but there are also many cases with strongly varying PL intensity as in Fig. 2(c). The simplest explanation for this dot-like PL along the nanotube are several quenching defects and confined PL only in-between the defects. The PL profile shown in Fig. 2(d) can indeed be modelled with five additional defects at the positions marked with the black arrows, using the same parameters for the exciton mobility. This simple assumption of complete quenching at five defects, can explain the dot-like PL, although the match between simulation and experiment is not perfect. It is conceivable that some defects might not quench excitons with an efficiency of 100%, and it is also discussed that defects could localize excitons which would then in turn lead to enhanced PL from the defects [35]. A strong indication of localized excitons should be a bright PL spot with a strong spectral red-shift due to the local state being lower in energy. Up to now, we could not observe this but it remains a very interesting question regarding the interaction of excitons and defects.

3.3 PL quenching at a localized defect site The data shown in Fig. 3 is based upon a spectroscopic image, where we recorded the complete optical spectrum at each of the 32×32 image pixels. In the example spectrum in Fig. 3(e), the Raman G-band at 700 nm and the PL peaks of two nanotubes with different chiralities can be seen. The peak at 930 nm originates from a DNA-wrapped (9,1) nanotube whereas the peak at 975 nm is characteristic for a DNA-wrapped (8,3) nanotube [36, 37]. The respective peak intensities derived from the spectra are mapped in Fig. 3(b–d). The topography in Fig. 3(a) shows a long and a short SWNT and some particles, probably excess DNA or some undefined dirt. The spectral information in (b) and (c) reveals that the long nanotube consists of two nanotubes with different chirality. The lower section is a (8,3) tube and the upper section is a (9,1) tube, that additionally shows a strong resonance Raman signal shown in (d). The short nanotube on the bottom left side is not visible in the optical images, because it is either metallic or emits beyond our detection window above 1050 nm.

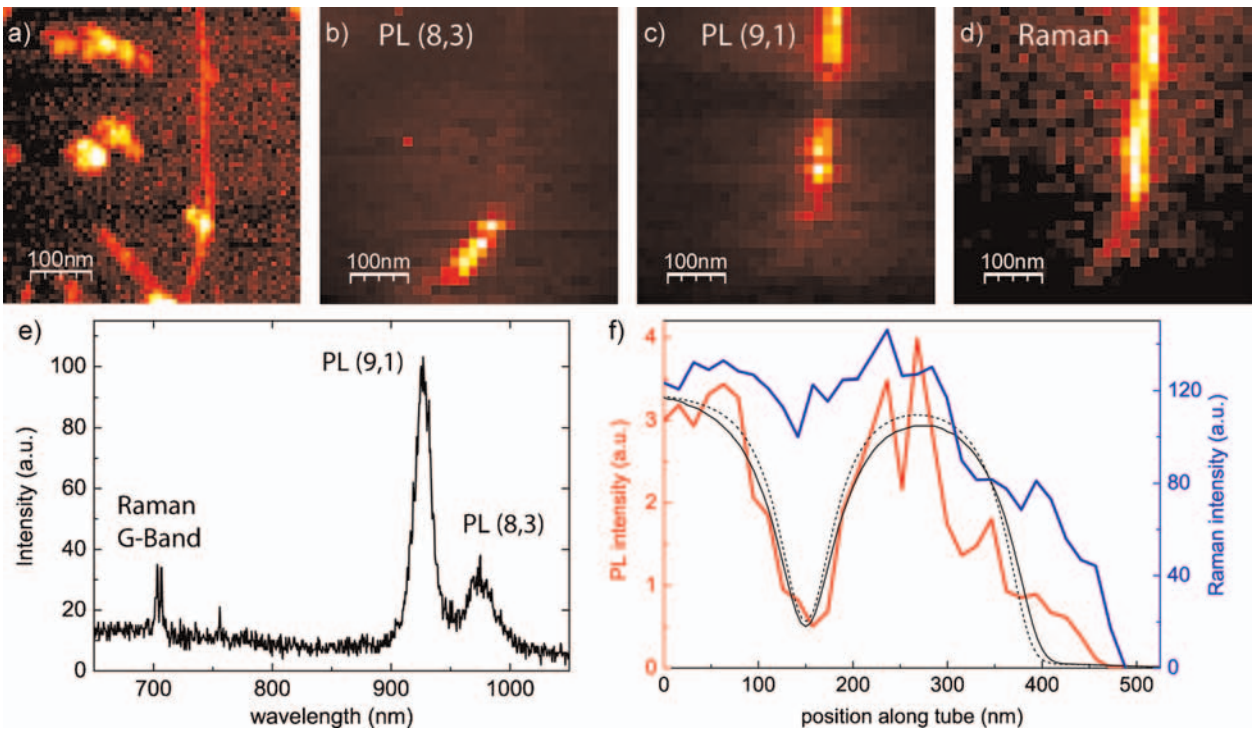

Figure 3 (online colour at: http://www.pss-b.com) Spectroscopic imaging of DNA-wrapped SWNTs. Images (b)–(d) were formed by acquiring spectra at every image pixel and subsequent analysis of the specific peaks. An example spectrum from the scan (e) clearly shows the Raman G-band and the PL peaks from a (8,3) and a (9,1) nanotube. (a) Topography. (b) PL intensity from the (8,3) nanotube at $\lambda = 975$ nm. (c) PL intensity from the (9,1) nanotube at $\lambda = 930$ nm. In the middle of this tube, the PL is quenched due to a localized defect. (d) Intensity of the Raman G-band at $\lambda = 700$ nm, much stronger for the resonant (9,1)-tube. (f) Cross-section of PL and Raman intensity along the (9,1)-tube and the simulated PL profile due to a single defect for a diffusion length of 100 nm (solid black line) or 80 nm (dashed line). The defect quenches the PL on a length of ~100 nm while the Raman signal remains unchanged, indicating no substantial damage of the nanotube. Near the defect position, the simulation fits best for a diffusion length of 100 nm, whereas a value of 80 nm results in a significantly narrower PL dip. Towards the end, a big particle (see topography) that can hinder tip-enhancement and contributions from the (8,3) nanotube, leads to the apparent mismatch with the modelling.

The PL and Raman signal along the (9,1) nanotube are plotted together in Fig. 3(f). From this and the images (c) and (d), it is apparent that the PL is quenched in the middle of this nanotube, while the Raman signal remains unchanged, confirming that the nanotube is not substantially damaged and the tip-enhancement is stable. We can assume a localized quenching defect at this location, but we cannot identify the microscopic origin, as e.g. chemisorbed oxygen or possibly related to the small dot on the nanotube visible in the topography. Unfortunately, the signal-to-noise ratio of the G′-band (peak in Fig. 3(e) at 760 nm), does not allow for analysis of its band shape in analogy to Ref. [35], in order to identify the defect type. When modelling the PL profile for a single quenching defect with $k_{\mathrm{nrad}} \rightarrow \infty$ and a diffusion length of 100 nm, we see very good agreement near the quenching site, regarding the length scale and relative amplitude of PL reduction. Using different diffusion length (e.g. 80 nm, 120 nm), the agreement is reduced and we thus extract a value of 100 ± 20 nm from the comparison between experiment and simulation. The lower end of the (9,1) nanotube is not well defined due to the big particle visible in the topography. The PL reduction towards this end does not agree with the simulation, because the particle could decrease PL enhancement, due an increased tip-sample distance, while the actual position of the end is also not clear from the optical data, due to some crosstalk from the (8,3) PL and Raman signals.

In summary, based upon near-field PL measurements, we determined a value of 100 ± 20 nm for the exciton diffusion length, in good agreement with recent confocal measurements [13, 14]. Thus, TENOM can directly visualize the effect of exciton diffusion. Using an exciton lifetime τ in the order of 5–20 ps [8], we derive a diffusion coefficient of 2.5–10 cm^2/s. By modelling and simulating the imaging and exciton diffusion process, we can reproduce the experimental near-field images, taking into account far-field background, confinement of tip-enhancement and modified decay rates due to the tip. These simulations are an important tool to study, e.g. exciton mobility in carbon nanotubes and extract values for diffusion length or tip-enhancement factors. Future time-resolved near-field measurements revealing e.g. the enhanced decay rates in the vicinity of the tip will further clarify these processes and also benefit from simultaneous simulations.

Acknowledgements The authors wish to acknowledge Nicolai Hartmann for sample support and Steffen Schmidt for SEM support. This work was funded by the Deutsche Forschungsgemeinschaft (DFG-HA4405/3-1) and the Nanosystems Initiative Munich (NIM). L.N. acknowledges support from DOE (grant DE-FG02-05ER46207).

References

[1] A. Jorio, M. S. Dresselhaus, and G. Dresselhaus (Eds.) Carbon Nanotubes (Springer, Berlin/Heidelberg, 2008), Vol. 111.

[2] P. Avouris, M. Freitag, and V. Perebeinos, Nature Phot. **2**, 341–350 (2008).

[3] E. Chang, G. Bussi, A. Ruini, and E. Molinari, Phys. Rev. Lett. **92**, 196401 (2004).

[4] C. D. Spataru, S. Ismail-Beigi, L. X. Benedict, and S. G. Louie, Phys. Rev. Lett. **92**, 077402–077405 (2004).

[5] A. Hagen, M. Steiner, M. B. Raschke, C. Lienau, T. Hertel, H. Qian, A. J. Meixner, and A. Hartschuh, Phys. Rev. Lett. **95**, 197401–197404 (2005).

[6] F. Wang, G. Dukovic, L. E. Brus, and T. F. Heinz, Phys. Rev. Lett. **92**, 177401–177404 (2004).

[7] Y. Z. Ma, J. Stenger, J. Zimmermann, S. M. Bachilo, R. E. Smalley, R. B. Weisman, and G. R. Fleming, J. Chem. Phys. **120**, 3368 (2004).

[8] T. Gokus, A. Hartschuh, H. Harutyunyan, M. Allegrini, F. Hennrich, M. Kappes, A. A. Green, M. C. Hersam, P. T. Araujo, and A. Jorio, Appl. Phys. Lett. **92**, 153116 (2008).

[9] S. Berciaud, L. Cognet, and B. Lounis, Phys. Rev. Lett. **101**, 077402 (2008).

[10] H. Qian, C. Georgi, N. Anderson, A. A. Green, M. C. Hersam, L. Novotny, and A. Hartschuh, Nano Lett. **8**, 1363–1367 (2008).

[11] H. Qian, P. T. Araujo, C. Georgi, T. Gokus, N. Hartmann, A. A. Green, A. Jorio, M. C. Hersam, L. Novotny, and A. Hartschuh, Nano Lett. **8**, 2706–2711 (2008).

[12] H. Qian, C. Georgi, N. Anderson, A. A. Green, M. C. Hersam, L. Novotny, and A. Hartschuh, Phys. Status Solidi B **245**, 2243–2246 (2008).

[13] L. Cognet, D. T. Tysboulski, J.-D. R. Rocha, C. D. Doyle, J. M. Tour, and R. B. Weisman, Science **316**, 1465–1468 (2007).

[14] C. Georgi, N. Hartmann, T. Gokus, A. A. Green, M. C. Hersam, and A. Hartschuh, Chem. Phys. Chem. **9**, 1460–1463 (2008).

[15] A. Hartschuh, H. Qian, A. J. Meixner, N. Anderson, and L. Novotny, Nano Lett. **5**, 2310–2313 (2005).

[16] S. Kawata, V. M. Shalaev, Eds. Tip enhancement in Advances in Nano-Optics and Nano-Photonics (Elsevier, Amsterdam, 2007, Chap 5, pp. 157–175).

[17] A. Hartschuh, E. J. Sánchez, X. S. Xie, and L. Novotny, Phys. Rev. Lett. **90**, 095503–095504 (2003).

[18] A. Hartschuh, Angew. Chem., Int. Ed. **47**, 8178–8198 (2008).

[19] K. Karrai and R. D. Grober, Appl. Phys. Lett. **66**, 1842–1844 (1995).

[20] M. S. Arnold, S. I. Stupp, and M. C. Hersam, Nano Lett. **5**, 713–718 (2005).

[21] M. S. Arnold, A. A. Green, J. F. Hulvat, S. I. Stupp, and M. C. Hersam, Nat. Nanotechnol. **1**, 60–65 (2006).

[22] A. A. Green and M. C. Hersam, Mater Today **10**, 59–60 (2007).

[23] M. Zheng, A. Jagota, E. D. Semke, B. A. Diner, R. S. Mclean, S. R. Lustig, R. E. Richardson, and N. G. Tassi, Nat. Mater. **2**, 338–342 (2003).

[24] M. S. Dresselhaus, G. Dresselhaus, R. Saito, and A. Jorio, Phys. Rep. **409**, 47–99 (2005).

[25] A. Rajan, M. S. Strano, D. A. Heller, T. Hertel, and K. Schulten, J. Phys. Chem. B **112**, 6211–6213 (2008).

[26] A. De Vita, J. C. Charlier, X. Blase, and R. Car, Appl. Phys. A. **68**, 283–286 (1999).

[27] D. L. Carroll, P. Redlich, P. M. Ajayan, J. C. Charlier, X. Blase, A. De Vta, and R. Car, Phys. Rev. Lett. **78**, 2811–2814 (1997).

[28] J. Hafner, C. L. Cheung, and C. M. Lieber, J. Am. Chem. Soc. **121**, 9750 (1999).
[29] S. J. Tans and C. Dekker, Nature **404**, 834–835 (2000).
[30] F. Wang, G. Dukovic, E. Knoesel, L. E. Brus, and T. F. Heinz, Phys. Rev. B **70**, 241403 (2004).
[31] V. Perebeinos and P. Avouris, Phys. Rev. Lett. **101**, 057401 (2008).
[32] S. Kühn, U. Hakanson, L. Rogobete, and V. Sandoghdar, Phys. Rev. Lett. **97**, 017402 (2006).
[33] L. Novotny and B. Hecht, Principles of Nano-Optics (Cambridge University Press, Cambridge, 2006).
[34] H. G. Frey, S. Witt, K. Felderer, and R. Guckenberger, Phys. Rev. Lett. **93**, 200801–200804 (2004).
[35] I. O. Maciel, N. Anderson, M. A. Pimenta, A. Hartschuh, H. Qian, M. Terrones, H. Terrones, J. Campos-Delgado, A. M. Rao, L. Novotny, and A. Jorio, Nat. Mater. **7**, 878 (2008).
[36] S. M. Bachilo, M. S. Strano, C. Kittrell, R. H. Hauge, R. Smalley, and R. B. Weisman, Science **298**, 2361–2366 (2002).
[37] E. S. Jeng, A. E. Moll, A. C. Roy, J. B. Gastala, and M. S. Strano, Nano Lett. **6**, 371–375 (2006).

